Effect Comparison of Different Conductor Widths in Magnetic Dam for Protection of NI REBCO Pancake Coils

Takanobu Mato and So Noguchi, *Member, IEEE*

***Abstract*— One of the most challenging problems of no-insulation (NI) REBCO pancake coils is mechanical and thermal protection. Particularly, pancake coils suffer high stress during a local-normal state transition (quench event). One solution is a magnetic dam, which is merely NI windings with a few turns. The effectiveness of magnetic dams by 4-mm-wide NI windings was demonstrated numerically in the previous study. The effectiveness would be different when the REBCO tapes with different widths are employed. Therefore, in this paper, the electromagnetic behaviors of NI REBCO pancake coils with the magnetic dam of 12-mm-wide REBCO tape are investigated numerically. The charging and the normal-state transition are simulated. It is demonstrated that the 4-mm-wide magnetic dam works more effectively due to the less screening current in the 4-mm-wide magnetic dam than the 12-mm-wide magnetic dam in this case.**

***Index Terms*—Magnetic dam, no-insulation, REBCO magnet, mechanical protection, quench.**

I. Introduction

In recent years, magnet performances have been increasing, and then a world-record DC field of 45.5 T has been generated [1]. The record is attributed to the use of the rare-earth barium copper oxide (REBCO) tape with a high critical field [2] and a no-insulation (NI) winding method [3]. The NI technology pushed the boundary of the magnet technology, enhancing the thermal stability due to the current sharing property between turns.

The high-field magnets have been facing mechanical challenges as the next problems. The high-field magnets experience strong Lorentz's force due to the high magnet field and the large operating current. As a matter of fact, the mechanical deformations of REBCO coils were found after the high field generation [4]-[6]. There are several possible mechanisms for mechanical deformation. One mechanism is the screening current effect. During the magnet excitation, the REBCO tape rotates, so that the REBCO tape width direction is identical to the field angle [7]-[11]. Another possibility is the large current accumulation during the normal-state transition (quench) [12]. When a REBCO pancake coil turns to a normal state, *i.e.*, the normal-state transition is triggered, the adjacent healthy pancake coils receive large energy from the normal-transitioned pancake coil, in the form of an induced current. The largely induced current may lead to hoop stresses beyond the yield stress of the REBCO tape [13], [14].

To reduce the hoop stress during the normal-state transition, the technique called "*magnetic dam*" has been proposed and investigated [15]-[17]. This technique was adopted in the actual high-field magnet to protect the superconducting magnet [18]. The magnetic dam is a copper ring or REBCO tape windings that are not energized. Some of the energy is transferred from the normal-state-transitioned coil to the magnetic dam during a normal-state transition event, and the maximum current of the adjacent healthy coils can be reduced. Fig. 1 shows the magnetic dam using REBCO tapes. Previously, the magnetic dam with 4-mm-wide winding was proven to be effective for magnet protection by numerical analysis [16]. The effectiveness of the magnetic dam with REBCO tapes with different widths would be different, for example, due to screening current distributions, arrangement of the magnetic dam, and magnetic coupling intensity. Therefore, in this paper, we investigate the magnetic dam with 12-mm REBCO tapes. The electromagnetic behaviors are investigated with the partial element equivalent circuit (PEEC) model [17], [18]. It can well represent the current distribution in the radial-axial plane. First, the magnet is charged, and then the local-normal-state transition is simulated. Three cases are compared: without a magnetic dam, with a 4-mm-wide magnetic dam, and with a 12-mm-wide one.

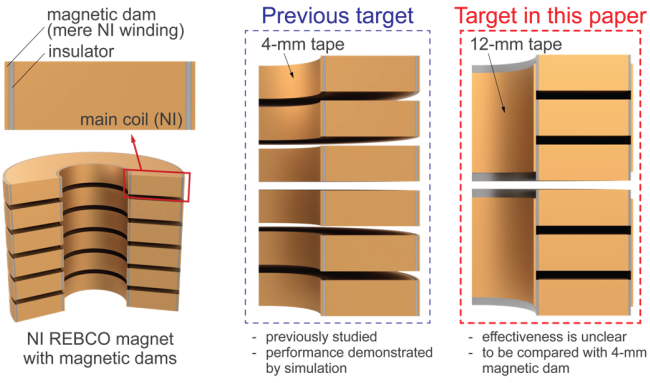

Fig. 1. Schematic illustration of magnetic dams with 4-mm -wide tapes and 12-mm-wide tapes.

Manuscript received. This work was supported by the JSPS KAKENHI under Grant No. 22KJ0104. (Corresponding author: Takanobu Mato.)

T. Mato and S. Noguchi were with Graduate School of Information Science and Technology, Hokkaido University, Sapporo, 060-0814 Japan (e-mail: e-mail: mato@em.ist.hokudai.ac.jp, noguchi@ssi.ist.hokudai.ac.jp).

Color versions of one or more of the figures in this article are available online at http://ieeexplore.ieee.org

Digital Object Identifier will be inserted here upon acceptance.

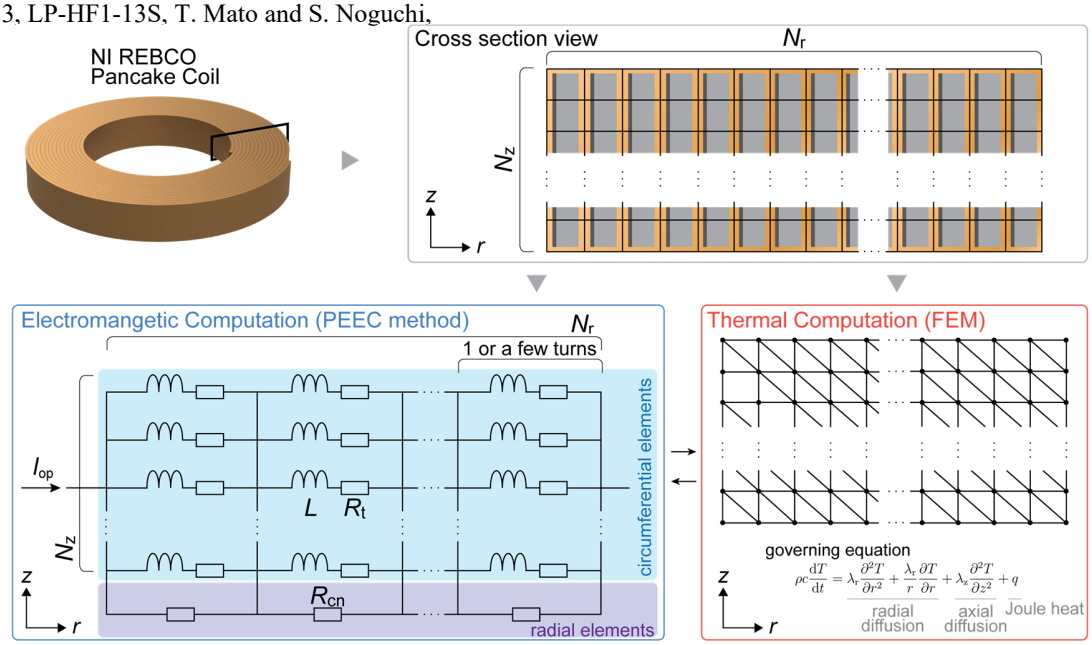

Fig. 2. Simulation model based on PEEC model for electromagnetic calculation and FEM model for thermal calculation. An NI REBCO pancake coil is divided along radial and axial direction. Both circuit and thermal simulations are conducted in axisymmetric coordinate system.

II. Simulation Model

Fig. 2 shows the simulation model used in this paper. As an electromagnetic model, the PEEC model was used [19], [20]. The NI REBCO pancake coil is subdivided into small element circuits, finely meshed in a radial-axial plane. The PEEC is able to model screening currents. The screening currents would be an important consideration, particularly in the case of wide REBCO tapes such as 12-mm-wide REBCO tape. Each small element consists of the circumferential inductance L and the REBCO tape resistance R_t. The turn-to-turn contact resistance R_c is connected in parallel with the circumferential element, assumed to be uniformly distributed in a turn. Thus, the governing equation of the circuit computation is

$$\sum_i \sum_j L_{ij} \frac{\mathrm{d}I_{t,ij}}{\mathrm{d}t} + R_{t,ij} I_{t,ij} = R_{cn,j} I_{cn,j} \qquad (1)$$

TABLE I
Coil Specifications and Operation Parameters

Parameters	Values
Main coil	
I.D.; OD.; Height [mm]	14.7; 34.7; 29
Number of single pancake coils	6
Number of turns of single pancake	200
Operating current [A]	300
Contact resistivity [μΩ·cm^2]	70
Magnetic dam	
(inner winding) I.D.; O.D. [mm]	14; 14.5
(outer winding) I.D.; O.D. [mm]	34.9; 35.4
Number of turns	5
Operating current [A]	0
REBCO tape width [mm]	4 or 12
Contact resistivity [μΩ·cm^2]	70
Operating temperature [K]	4.2
Field by outer resistive magnet [T]	31.2

$$\sum_i I_{t,ij} + I_{cn,j} = I_{op} \qquad (2)$$

$$i \in \{1,2,\dots,N_z\}, \qquad j \in \{1,2,\dots,N_r\}$$

where, I_t, I_{cn}, I_{op}, N_z, and N_r are the azimuthal current, the current flowing in the contact resistance, the operating current, the number of axial elements, and the number of radial elements, respectively. The REBCO layer resistances are calculated from an n-value index model, in which n-value is constant at 25 in this simulation. Here, the field angle dependence on the critical current is considered as well as the field intensity and temperature dependence by using the fitting formula as shown in [21]. The inductances are calculated with the formula shown in [22]. It is also noted that the contact resistivity is assumed uniform in the pancake coils.

The electromagnetic computation is coupled with the thermal computation [23]. The governing equation is shown as follows:

$$\rho c \frac{\mathrm{d}T}{\mathrm{d}t} = \lambda_r \frac{\partial^2 T}{\partial r^2} + \frac{\lambda_r}{r}\frac{\partial T}{\partial r} + \lambda_z \frac{\partial^2 T}{\partial z^2} + q \qquad (3)$$

where, ρ, c, T, t, r, z, λ_r, λ_z, and q are the mass density, the heat capacity per unit mass, the temperature, the time, the radial coordinate, the axial coordinate, the heat conductivities along the radial and the axial directions, and the Joule heat per unit volume, respectively. The governing equation is solved by the finite element method (FEM) under an adiabatic condition. Here, the Joule heat per unit volume is given from the current distribution by circuit simulation. We considered temperature dependences of the electrical and thermal properties by changing them according to the temperature. The used properties are referred from [24], [25].

III. Charging Simulation

Table I lists the specifications of the simulated NI REBCO pancake coils. The main coils are placed in the outer resistive

magnet [26]. Table I also lists the specifications of magnetic dams. The arrangements of the magnetic dams are seen in Fig. 1. The power source is not connected to the magnetic dams but to the main coils. Here, we adopted the contact resistivity of 70 μΩ·cm^2, which was referred from [27]. In [27], the contact resistance was measured at 77 K (self-field); however, it would change depending on the conditions such as the operating temperature and the magnetic field. Since we do not know the exact values under the simulated conditions, the assumption of 70 μΩ·cm^2 is made in this paper. First, the insert NI REBCO coil is charged, and then the normal-state transition is simulated. It is assumed that the coil temperature is constant at 4.2 K during the charging, and variable in normal-state transition simulation.

Fig. 3 shows the axial field at the magnet center during the insert charging and the operating current increasing at 1 A/s. Here, the outer resistive magnet is charged in advance. The magnetic field without the magnetic dam reaches 42.24 T, while 42.15 T with the 4-mm-wide magnetic dam and 41.97 T with the 12-mm-wide one. The magnetic dam using wide-width REBCO tapes deteriorates the field intensity. Fig. 4 is the current distribution at 600 s in Fig. 3. The current penetrates the coils from the top and bottom edges of each pancake of the main coils. Due to the magnetic dams, the screening current distributions on the main coils differ, especially on SP2 and SP5. The screening currents are also induced in the magnetic dams. In the magnetic dams, the induced screening currents entirely distribute sufficiently inside the tapes in both cases of the 12-mm-wide and 4-mm-wide magnetic dams.

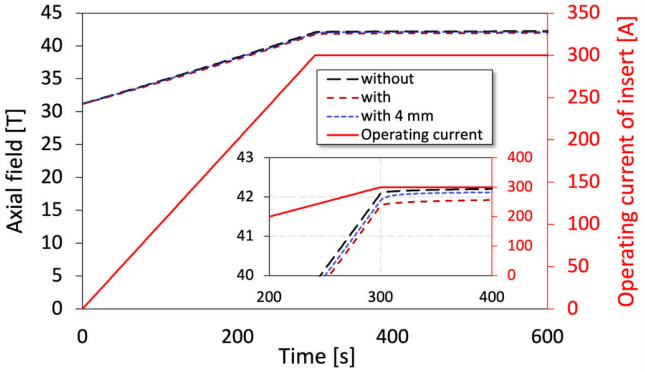

Fig. 3. Axial field for three cases and operating current of main coil.

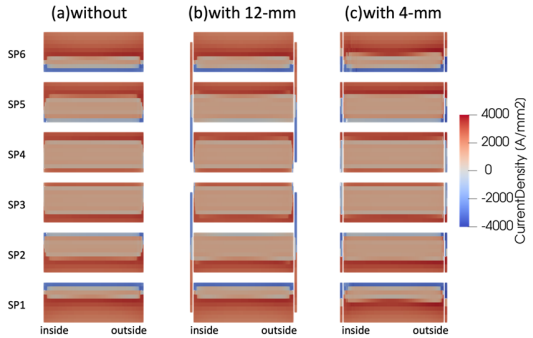

Fig. 4. Azimuthal current distribution at 600 s in Fig. 3: (a) without magnetic dam, (b) with 12-mm magnetic dam, and (c) with 4-mm magnetic dam.

IV. Normal-State Transition Simulation

A. Current density and temperature distributions

Next, we simulate the normal-state transition. The initial current distributions are as shown in Fig. 4. The most bottom pancake coil (SP1) is assumed to turn into a normal state as a worst-case scenario. Fig. 5 shows the current density and temperature distributions during the normal-state transition. Here, the time of "0 ms" means the time to start the SP1 turning to the normal state. In the case without the magnetic dam, a large current is induced at the bottom of the SP2 at 0.12 ms. Then, the currents propagate towards the top edge of the SP2 like a "wave." At 1.0 ms, the current wave reaches slightly up to the bottom edge of the SP3. It is also seen that the high-temperature region expands.

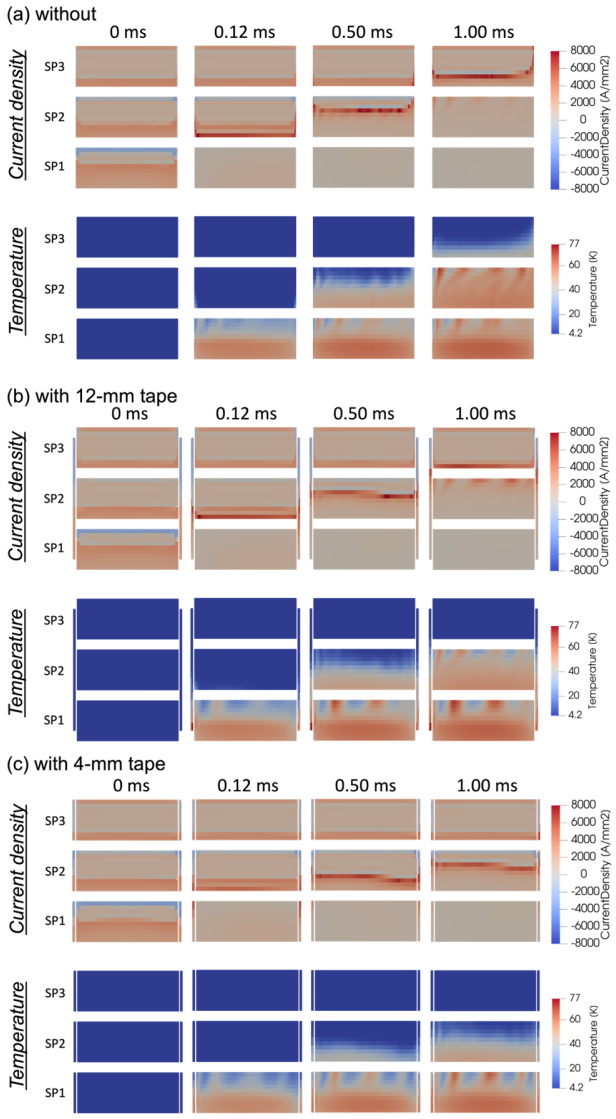

Fig. 5. Current density and temperature distributions during normal-state transition in cases (a) without magnetic dam, (b) with 12-mm magnetic dam, and (c) with 4-mm magnetic dam. It is assumed that the SP1 turns to normal state.

With the 12-mm-wide magnetic dam [Fig. 5(b)], the distributions are different. At 0.12 ms, the current wave more evenly distributes on the bottom edge of SP2 when compared with Fig. 5(a). The current propagation develops faster at the inner side and slower at the outer side in the main coils. This is because some of the energy is transferred to the bottom of the 12-mm-wide windings. A high temperature at the bottom of the 12-mm windings can be observed, caused by the large Joule heating after the transition to the normal state of SP1.

In the case of the 4-mm-wide magnetic dam, the current wave propagates in almost the same manner as the 12-mm-wide magnetic dam, but slower than that. It is noted that the currents remain a relatively long time on the magnetic dam next to SP1, where the screening current flows in an opposite direction to the main coil current at $t = 0$. This means that the current margin of the 4-mm-wide magnetic dam next to SP1 is larger than the 12-mm magnetic dam.

B. BJR transition

The hoop stress is simply estimated using *BJR* relation as

$$\sigma_{\mathrm{hoop}} = B_z JR \qquad (4)$$

where B_z, J, and R are the axial field, the current density, and the radius of elements, respectively. The *BJR* calculation is applied to each circuit element and the maximum *BJR*s are plotted as a function of time in Fig. 6. It should be noted that the estimated *BJR* stresses are very high beyond the permissible tensile strength of the tape since the stresses are just computed at each circuit element. Yet, there is a possibility that local strong stress causes local mechanical damage. The actual stress would be less than the evaluated stress because the local concentrated stress is shared in REBCO tapes or a pancake coil. Also, the fluctuation is caused by the rough discretization in time. A detailed stress simulation is needed for accurate estimation.

Fig. 6(a) is the case without magnetic dams. The highest hoop stress in the entire transition is applied to the SP2 in the beginning. Each pancake coil experiences high hoop stress during the normal-state propagation. When the 12-mm-wide magnetic dam is installed [Fig.6(b)], the maximum *BJR* stress on SP2 is lowered by 25 % than that without magnetic dams. The energy of the SP1 is transferred to the 12-mm-wide magnetic dam just after the normal-state transition of the SP1. The effectiveness of the 12-mm-wide magnetic dam has been demonstrated. Fig. 6(c) is the case with the 4-mm-wide magnetic dam. The 4-mm-wide magnetic dam reduces the maximum *BJR* stresses more than the 12-mm-wide magnetic dam. As explained in the previous section, it can be attributed to the screening current distribution in the magnetic dam and the consequent current margin around the SP1, *i.e.* the most bottom 4-mm-wide magnetic dam sufficiently absorbs the magnetic energy from the SP1. Also, the speed of the normal-state propagation is significantly slowed down because the energy is well transferred.

V. Conclusion

The effectiveness of the 12- and 4-mm-wide magnetic dams are compared in this paper. Three cases are compared: without magnetic dams, with a 12-mm-wide magnetic dam, and a 4-mm-wide one. The simulation follows two steps to consider the screening current distribution: 1) charging of the magnet, and then 2) normal-state transition. As a charging result, the center magnetic field deteriorates due to the screening current in the magnetic dams. The 12-mm-wide magnetic dam reduces the reached center field more than the 4-mm-width case. From the normal-state transition simulation, the effectiveness of the magnetic dam is evaluated with the simple *BJR* relation. The results show that both 4- and 12-mm-wide magnetic dams effectively work so that the maximum *BJR* stresses are reduced, although the 4-mm-wide magnetic dam works more effectively. This could be due to the screening current distribution before the normal-state transition. The 12-mm-wide REBCO tape carries the large current around the normal-transitioned pancake (SP1). Thus the 12-mm-wide magnetic does not absorb the energy from the SP1 as much as the 4-mm-wide magnetic dam.

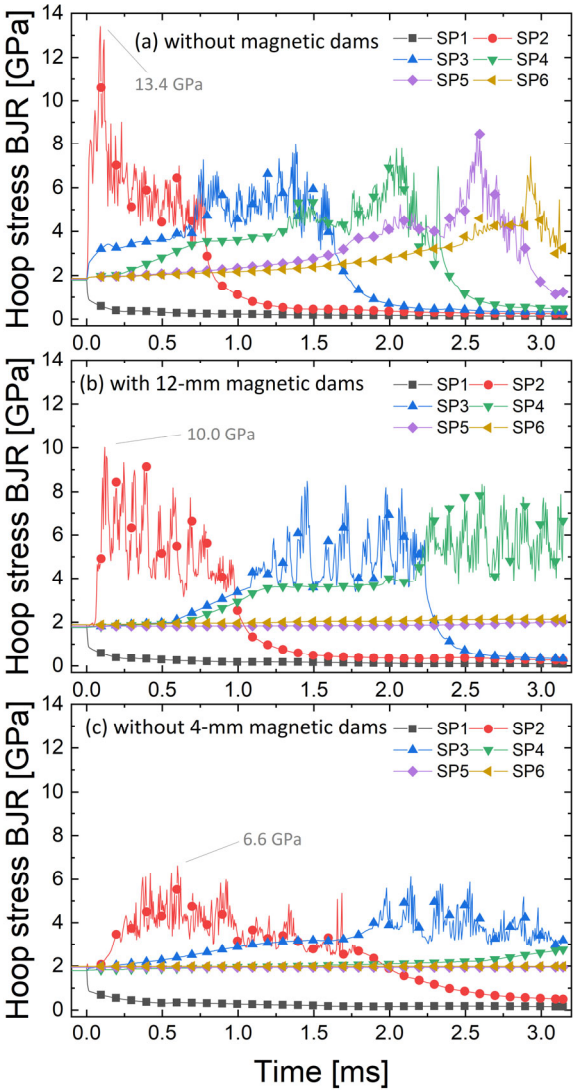

Fig. 6. *BJR* stress transition during normal-state transition in case (a) without magnetic dam, (b) with 12-mm magnetic dam, and (c) with 4-mm magnetic dam. The maximum *BJR* stresses in each pancake are plotted.

REFERENCES

[1] S. Hahn *et al*., "45.5-Tesla Direct-Current Magnetic Field Generated with a High-Temperature Superconducting Magnet," *Nature*, vol. 570, no. 7762, pp. 496–499, 2019.

[2] K. Wang *et al*., "Advances in Second-Generation High-Temperature Superconducting Tapes and Their Applications in High-Field Magnets," *Soft Sci*., vol. 2, no. 3, 2022.

[3] S. Hahn, D. K. Park, J. Bascuñán, and Y. Iwasa, "HTS Pancake Coils without Turn-to-Turn Insulation," *IEEE Trans. Appl. Supercond.*, vol. 21, no. 3, pp. 1592–1595, 2011.

[4] P. C. Michael *et al*., "Assembly and Test of a 3-Nested-Coil 800-MHz REBCO Insert (H800) for the MIT 1.3 GHz LTS/HTS NMR Magnet," *IEEE Trans. Appl. Supercond*., vol. 29, no. 5, 2019, Art. no. 4300706.

[5] Y. Suetomi *et al*., "Quench and Self-Protecting Behaviour of an Intra-Layer No-Insulation (LNI) REBCO Coil at 31.4 T," *Supercond. Sci. Technol*., vol. 34, no. 6, 2021, Art. no. 064003.

[6] X. Hu *et al*., "Analyses of The Plastic Deformation of Coated Conductors Deconstructed from Ultra-High Field Test Coils," *Supercond. Sci. Technol.,* vol. 33, 2020, Art. no. 095012.

[7] S. Noguchi, T. Mato, K. Kim, and S. Hahn, "Electromagnetic Behavior Simulation of REBCO Pancake Coils Considering REBCO Tape Rotation Under High Magnetic Field," *IEEE Trans. Appl. Supercond*., vol. 33, no. 5, 2023, Art. no. 4300405.

[8] Y. Yan, Y. Li, and T. Qu, "Screening Current Induced Magnetic Field and Stress in Ultra-High-Field Magnets Using REBCO Coated Conductors," *Supercond. Sci. Technol*., vol. 35, 2021, Art. no. 014003.

[9] D. Kolb-Bond, M. Bird, I. R. Dixon, and T. Painter, "Screening Current Rotation Effects: SCIF and Strain in REBCO Magnets," *Supercond. Sci. Technol.*, vol. 34, no. 9, 2021, Art. no. 095004.

[10] H. Ueda, K. Naito, R. Inoue, and S. Kim, "Deformation Analysis of No-Insulation REBCO Coils Considering Turn-to-Turn Contact Configuration," *IEEE Trans. Appl. Supercond*., vol. 32, no. 6, 2022, Art. no. 4604205.

[11] G. Dilasser, P. Fazilleau, and P. Tixador, "Experimental Measurement and Numerical Simulation of the Screening Current-Induced Field Decay in a Small ReBCO Coil," *IEEE Trans. Appl. Supercond*., vol. 27, no. 4, 2017, Art. no. 4900104.

[12] R. Miyao, H. Igarashi, A. Ishiyama, and S. Noguchi, "Thermal and Electromagnetic Simulation of Multistacked No-Insulation REBCO Pancake Coils on Normal-State Transition by PEEC Method," *IEEE Trans. Appl. Supercond.*, vol. 28, no. 3, 2018, Art. no. 4601405.

[13] C. C. Clickner *et al.*, "Mechanical properties of pure Ni and Ni-alloy substrate materials for Y–Ba–Cu–O coated superconductors," *Cryogenics*, vol. 46, no. 6, pp. 432–438, Jun. 2006.

[14] C. Barth, G. Mondonico, and C. Senatore, "Electro-Mechanical Properties of REBCO Coated Conductors from Various Industrial Manufacturers at 77 K, Self-Field And 4.2 K, 19 T," *Supercond. Sci. Technol*., vol. 28, no. 4, 2015, Art. no. 045011.

[15] S. An *et al*., "A Feasibility Study on 'Magnetic Dam' to Absorb Magnetic Energy in NI HTS Magnet During Quench," *IEEE Trans. Appl. Supercond*., vol. 30, no. 4, 2020, Art. no. 4701705.

[16] T. Mato, S. Hahn, and S. Noguchi, "Mechanical Damage Protection Method by Reducing Induced Current in NI REBCO Pancake Coils During Quench Propagation," *IEEE Trans. Appl. Supercond*., vol. 31, no. 5, 2021, Art. no. 4602405.

[17] P. Fazilleau, F. Borgnolutti, and T. Lécrevisse, "Protection Design for a 10-T HTS Insert Magnet," *IEEE Trans. Appl. Supercond*., vol. 26, no. 3, 2016, Art. no. 4700705.

[18] P. Fazilleau, G. Aubert, C. Berriaud, B. Hervieu, and P. Pugnat, "Role and Impact of the Eddy Current Shield in the LNCMI-G Hybrid Magnet," *IEEE Trans. Appl. Supercond*., vol. 26, no. 4, 2016, Art. no. 4301305.

[19] S. Noguchi, "Electromagnetic, Thermal, and Mechanical Quench Simulation of NI REBCO Pancake Coils for High Magnetic Field Generation," *IEEE Trans. Appl. Supercond*., vol. 29, no. 5, p. 4602607, Aug. 2019.

[20] K. Ota, S. Kokubo, A. Ishiyama, H. Ueda, and S. Noguchi, "Screening Current-Induced Magnetic Field Analysis of No-Insulation Coils which Uses Bidirectional Split-Circuit Screening Current Magnetic Field Analysis (Part 1): Formulation," *Abstracts of CSSJ Conference*, vol 104, pp. 114, 2022.

[21] H. Ueda *et al*., "Numerical Simulation on Magnetic Field Generated by Screening Current in 10-T-Class REBCO Coil," *IEEE Trans. Appl. Supercond*., vol. 26, no. 4, 2016, Art. no. 4701205.

[22] S. I. Babic and C. Akyel, "New Analytic-Numerical Solutions for the Mutual Inductance of Two Coaxial Circular Coils with Rectangular Cross Section in Air," *IEEE Trans. Magn.*, vol. 42, no. 6, pp. 1661–1669, 2006.

[23] T. Wang *et al*., "Analyses of Transient Behaviors of No-Insulation REBCO Pancake Coils During Sudden Discharging and Overcurrent," *IEEE Trans. Appl. Supercond.*, vol. 25, no. 3, 2015, Art. no. 4603409.

[24] Cryogenics and Superconductivity Society of Japan, "Handbook of superconductivity and cryogenics," [Online]. Available: https://csj.or.jp/handbook/index.html, Accessed: Sep. 21, 2023.

[25] J. Lu, E.S. Choi, and H.D. Zhou, "Physical Properties of Hastelloy C-276™ at Cryogenic Temperatures," *J. Appl. Phys*., vol. 103, no. 6, 2008, Art. no. 064908.

[26] National High Magnetic Field Laboratory, "31 Tesla, 50 mm Bore Magnet (Cell 7)," [Online]. Available: https://nationalmaglab.org/user-facilities/dc-field/magnets-instruments/resistive-magnets/31-tesla-cell-7/, Accessed: Sep. 21, 2023.

[27] X. Wang *et al.*, "Turn-to-Turn Contact Characteristics for An Equivalent Circuit Model of No-Insulation ReBCO Pancake Coil," *Supercond. Sci. Technol.*, vol. 26, no. 3, 2013, Art. no. 035012.